

Infrared Thermography as a Non-destructive Testing Solution for Thermal Spray Metal Coatings

Paolo E. Santangelo¹ · Giulio Allesina¹ · Giovanni Bolelli¹ · Luca Lusvarghi¹ · Ville Matikainen² · Petri Vuoristo²

Submitted: 11 July 2017 / in revised form: 1 September 2017 / Published online: 15 September 2017
© ASM International 2017

Abstract In this work, an infrared (IR) thermographic procedure was evaluated as a non-destructive testing tool to detect damage in thermal spray metallic coatings. As model systems, polished HVOF- and HVAF-sprayed Fe-based layers deposited onto steel plates were employed. Damage by external-object impingement was simulated through a cyclic impact-test apparatus, which induced circumferential and radial cracks across all model systems, and interface cracks of different sizes in distinct samples. Damaged and undamaged plates were bulk-heated to above 100 °C using an IR lamp; their free-convection cooling was then recorded by an IR thermocamera. The intentionally induced defects were hardly detectable in IR thermograms, due to IR reflection and artificial “hot” spots induced by residuals of transfer material from the impacting counterbody. As a micrometer-thin layer of black paint was applied, surface emissivity got homogenized and any artifacts were effectively suppressed, so that failed coating areas clearly showed up as “cold spots.” This effect was more apparent when large interface cracks occurred. Finite-element modeling proved the physical significance of the IR-thermography approach, showing that failed coating areas are cooled by surrounding air faster than they are heated by conduction from the hot substrate, which is due to the insulating effect of cracks.

Keywords finite element modeling · high-velocity air fuel (HVAF) · high-velocity oxy fuel (HVOF) · impact testing · non-destructive inspection

Introduction

Thermal spray coatings are employed in a variety of fields: gas turbines (Ref 1-3), steelmaking and papermaking industry, petrochemical plants, pumps and hydraulic machinery, etc. (Ref 4). For the above-mentioned applications, thermal spray processes exhibit high versatility and productivity and are often preferred over several other coating technologies. However, their performance may be limited by cohesive strength—determined by their lamellar structure (Ref 5)—and by adhesive strength to the substrate through mechanical interlocking (Ref 6, 7) to its roughened surface.

So, it is crucial to monitor the coatings throughout their operating life using non-destructive inspection techniques: Early detection of adhesive and/or cohesive cracks may likely prevent catastrophic failures. Together with ultrasonic and laser-ultrasonic testing (Ref 8, 9), thermographic techniques (Ref 9) feature significant potential advantages in detecting subsurface defects thanks to their simplicity and the relatively low cost. The most recognized implementation of these methods consists of monitoring the condition of thermal barrier coating (TBC) systems (Ref 10-15): an infrared (IR) thermocamera records the temperature trend of a coated surface subjected to a heat pulse applied through flash lamps (Ref 16). The onset and progression of delamination cracks in the partially stabilized zirconia-based ceramic topcoat, close to the interface with the bond coat, is the main failure mechanism during thermal cycling (Ref 17); it is driven by stress accumulation,

✉ Giovanni Bolelli
giovanni.bolelli@unimore.it

¹ Dipartimento di Ingegneria “Enzo Ferrari”, Università degli Studi di Modena e Reggio Emilia, Via P. Vivarelli 10, 41125 Modena, Italy

² Laboratory of Materials Science, Faculty of Engineering Sciences, Tampere University of Technology, Korkeakoulunkatu 6, Tampere, Finland

because of the progressively increasing thickness of the thermally grown oxide (TGO), and of the mismatch in thermal expansion coefficients between the various layers. The low thermal conductivity of the ceramic topcoat allows detecting “hot spots” where the coating does not effectively dissipate the heat pulse toward the substrate as a result of a delamination crack.

Similar uses of pulsed thermography refer to other ceramic coatings (Ref 16, 18), which also present low thermal conductivity. The potential applicability to other coating materials seems to be more complex, since “hot spots” might be harder to detect because of higher thermal conductivity. For instance, the detection of interface defects between fiber-reinforced polymer composite layers and aluminum substrates in multilayered aeronautical structures is reportedly difficult because of the high lateral thermal conductivity of the composite. Indeed, this means a “hot spot” hardly develops as heat is preferentially dissipated to the sides rather than across the thickness (Ref 19). Problems also arose with thermal spray aluminum coatings onto steel substrates (Ref 20). Nonetheless, significant attempts have been made to use thermography with thermal spray metals and hardmetals (Ref 20–23), including delamination-crack detection in coated Pelton turbines (Ref 24).

The present work aims at validating IR thermography as a non-destructive inspection tool to detect delamination cracks in thermally sprayed metallic coatings. It specifically focuses on demonstrating a particularly simple implementation of the method, which does not require complex instrumentation, such as flash lamps or laser heating (Ref 25). It is, therefore, easy to implement both in industry, to detect failed components, and in fundamental research for highlighting subsurface damage after lab-scale tests. The approach relies on bulk heating of the component using a simple heat source. This was originally proposed in (Ref 26) for ceramic TBCs and proved as effective as the flash-heating method; its applicability is here extended to metal coatings.

Materials and Methods

Sample Preparation and Testing

In this study, four thermally sprayed Fe-based alloy coatings were employed, which were previously characterized (Ref 27). Fe-31Cr-12Ni-3.6B-0.6C (wt.%) and Fe-31Cr-12Ni-2Mo-3.6B-0.6C (wt.%) feedstock powders were selected, and each was sprayed onto one face of low-carbon steel (Fe52) plates or disks (5 mm thickness) both by the high-velocity oxygen fuel (HVOF) and by the high-velocity air fuel (HVAF) thermal spray techniques. Details on

feedstock powders, substrate preparation method and deposition parameters can be found in (Ref 27). Plates and disks were subsequently cut into samples with a characteristic length of about 25 mm. All samples were ground with SiC papers and polished with 3- μ m diamond slurry to a mirror-like finish (arithmetic mean roughness $<0.1 \mu\text{m}$), which corresponds to the typical specification for this type of hard, wear-resistant coatings in usual applications such as paper- and steelmaking rolls, journal bearings, rotary seal joints, ball valves (Ref 4). A thickness of 300–600 μm was eventually achieved after grinding and polishing.

Defects were induced by subjecting the coatings to cyclic impact testing. An X200Cr13 steel sphere (39 mm diameter) attached to an overall 1.4 kg mass was repeatedly dropped from an 80 mm height onto the polished sample surface. Linear ball bearings were employed to guide the drop assembly, thus allowing consistent and repeatable impact location, as described in detail in (Ref 28). This is intended to simulate damage by foreign objects impingement, a particularly dangerous occurrence for thermal spray coatings due to their limited adhesion strength in comparison, for example, with clad layers.

After 200 impact cycles at a frequency of 45 impacts/min, each sample was removed, inspected by optical microscopy and then employed for IR-thermography tests as described in detail in “[Thermographic Testing: Instrumentation and Procedure](#)” section. After IR-thermography analysis, samples were eventually subjected to destructive metallographic inspection. Notably, they were cold-mounted in epoxy resin, cut with a metallographic saw, ground and polished using SiC papers, 3- μ m diamond slurry and colloidal silica suspension, and observed by Field Emission Gun-Scanning Electron Microscopy (FEG-SEM, Nova NanoSEM 400 by FEI) to assess the actual extent of subsurface damage.

Thermographic Testing: Instrumentation and Procedure

Each sample was placed onto an insulating slab enabled to run along a rail (Fig. 1). As the first step, the coated face

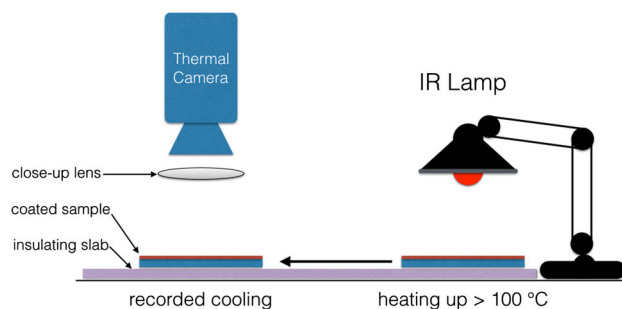


Fig. 1 Schematic of the IR-thermography experiment

was heated from above by an IR lamp for at least 5 min (300 s) until the surface temperature exceeded 100 °C. The sample was then quickly moved under the IR thermocamera (TVS-500 by Avio) used for inspection, the lens of which was set as parallel to the coated surface. The device is endowed with a micro-bolometric FPA (focal plane array) sensor (operating spectral band: 8–12 μm), an IEEE-1394 interface and automatic calibration (Ref 29–32). The cooling trend was recorded at 5 frames/s, and a close-up lens was also added to augment image resolution (1 pixel to 115 μm). As for the field of view, the employed thermocamera features a 240 × 320 pixel image size; the width and length of each acquired thermographic snapshot were 28 and 37 mm, respectively.

Two sets of experiments were run. First, untreated sample surfaces were analyzed imposing emissivity 0.20 in image post-processing. This value was chosen as representative of metal surfaces, which generally feature low emissivity (Ref 33). Notably, 0.20 was taken as a reasonable estimate arisen from the values for polished iron surfaces within the 8–14 μm wavelength range [0.21–0.28, (Ref 34)], even though well-established values for the coatings mentioned in “[Sample Preparation and Testing](#)” section do not appear available in the open literature.

Subsequently, a black-paint acrylic thin layer (thickness of micrometric order, but bigger than the maximum operating wavelength of the thermocamera) was also applied onto sample surfaces (Ref 30–32) to enhance IR absorption (blackbody promoting rapid heating) (Ref 30–32) and to avoid undesired reflection of surrounding irradiation and light from the interrogation region. Typical 0.95 emissivity value was set in image post-processing for black-coated samples (Ref 30–32). This method proved effective for a quantitative evaluation of the transient thermal history of solid substrates by IR thermography [± 0.8 °C total error (Ref 29, 31)] as a result of almost no external effects on an a priori known emissivity condition.

As inspired by previous works on IR thermography applied to dropwise cooling (Ref 29–32, 35), an attempt to emphasize crack visualization was made by manually releasing an ethanol droplet onto the black-painted sample surface. Ethanol spectral transmittance varies remarkably within the operating spectral range of IR thermocameras, oscillating between 1 and even below 0.2 (Ref 36), so it cannot be considered infrared-transparent at all. Therefore, quantitative measurements by IR thermography from above (Fig. 1)—as in the seminal work by Klassen et al. (Ref 35)—should account for ethanol emissivity in post-processing every image where the ethanol droplet is present. The variability connected with its transmittance implies that a quantitative analysis with imposed emissivity 0.95 can be performed on thermograms once the ethanol

droplet is fully evaporated. Ultimately, the ethanol droplet provides a localized, enhanced cooling effect.

Three IR-thermography test repeats were run for each of the four thermal spray coating configurations in both untreated and black-painted surface condition to verify repeatability of the proposed methodology. The temperature scale in the thermographic images presented here was adjusted to emphasize visualization of features of interest. So, the color bar spans over a temperature range between 10 and 35 °C; that range does not imply the absence of hotter or colder locations on the sample surface.

Finite-Element Approach

A planar, axisymmetric finite element (FE) model of a coated sample was developed to predict the temperature trend throughout cooling from an initial uniform temperature of 150 °C, approximately equal to the maximum temperature attained during IR heating of test samples. Symmetry of the sample cross section with respect to a generic plane perpendicular to the sample top surface was applied. The sample was assumed to have two internal defects: (1) a 10-μm wide circumferential crack, located 1.6 mm away from the symmetry axis and spanning 3/4 of the coating thickness, and (2) a 1.5-mm-long, 50-μm-thick interface crack (detail in Fig. 2a and overview in Fig. 2b). The computational domain was discretized using 8-node quadrilateral elements (Ref 37), as shown in Fig. 2. Approximately 50,000 elements were employed; finer grid size (~ 5 μm) was used in the vicinity of the cracks, where the larger temperature gradients and heat fluxes are expected. The largest element size within the coating—even in areas far from the cracks—did not exceed 25 μm, which is consistent with the coating thickness, while the element size was made grow up to 0.2 mm toward the bottom face of the substrate.

Inside the cracks, air was assumed to exchange heat only by conduction, since convective phenomena appear negligible if not very unlikely, due to the small gap size (Ref 33). Therefore, the heat diffusion equation (Ref 33) was implemented as representative of the heat distribution within all solid bodies (i.e., coating and substrate) and air inside the cracks:

$$\rho c \frac{\partial T}{\partial t} = \lambda \nabla^2 T \quad (\text{Eq 1})$$

where ρ is density, c is specific heat, T is temperature, t is time, and λ is thermal conductivity. Constant thermophysical properties were assumed in this model; notably, the thermophysical properties of air were taken from (Ref 38), while coating and substrate properties are summarized in Table 1. Specifically, an approximate coating density was imposed to account for the presence of slight porosity in the Fe-based alloy; its thermal conductivity was taken as

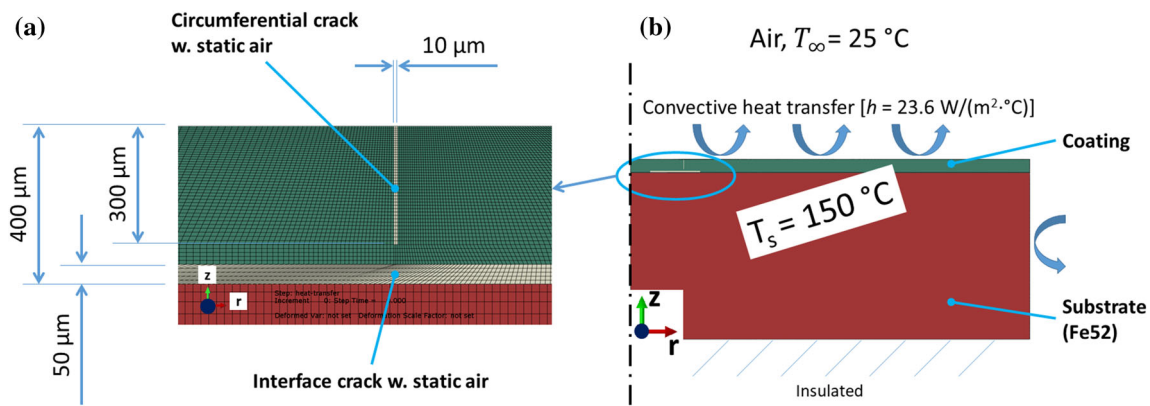


Fig. 2 FE computational domain and model of heat transfer across a coated sample having a transverse circumferential crack and an interface crack: detail of the cracks region and of the corresponding mesh (a) and overview with boundary conditions (b)

Table 1 Thermophysical properties of coating and substrate employed in the FE model

	ρ , kg/m ³	c , kJ/(kg °C)	λ , W/(m °C)
Coating	~7500	475	8 (Ref 33)
Substrate (Ref 37)	7850	475	46.6

equal to the value measured for thermally sprayed stainless steel (Ref 39).

The boundary conditions at the solid/solid and solid/gas (where gas refers here to air inside cracks) interfaces arise from the continuity of temperature and heat flux (Ref 33) along both the radial and through-thickness (axial) coordinates (Fig. 2):

$$T_{s1} = T_{s2}, T_s = T_g \tag{Eq 2}$$

$$\lambda_{s1} \frac{\partial T_{s1}}{\partial z} = \lambda_{s2} \frac{\partial T_{s2}}{\partial z}, \lambda_s \frac{\partial T_s}{\partial r} = \lambda_g \frac{\partial T_g}{\partial r}, \lambda_s \frac{\partial T_s}{\partial z} = \lambda_g \frac{\partial T_g}{\partial z} \tag{Eq 3}$$

where the subscript *s* refers to a solid body, *1* and *2* refer to the two solid bodies in contact with each other (i.e., coating and substrate), *g* refers to gas, *r* is the radial coordinate, and *z* is the axial coordinate. As previously mentioned and sketched in Fig. 2, this is a typical axisymmetric model using cylindrical coordinates, so all quantities are independent of the angular coordinate.

As for external boundary conditions, at the top and the side surfaces the coated structure exchanges heat by natural convection with surrounding air at 25 °C temperature, according to Eq 4, while the bottom surface is assumed to be adiabatic according to Eq 5 (no heat flux along the normal direction, Fig. 2), since in the actual implementation (Fig. 1) the coated body lies on an insulating slab:

$$\lambda_s \frac{\partial T_s}{\partial z} = h(T_{\text{surf}} - T_\infty), \lambda_s \frac{\partial T_s}{\partial r} = h(T_{\text{surf}} - T_\infty) \tag{Eq 4}$$

$$\frac{\partial T_s}{\partial n} = \frac{\partial T_s}{\partial z} = 0 \tag{Eq 5}$$

where *h* is the convective heat transfer coefficient, *T_{surf}* is the solid surface temperature, *T_∞* is free-stream air temperature, and *n* is the coordinate normal to a generic surface.

The convective heat transfer coefficient at the interface between the solid plate and the surrounding air was obtained by calculating the Nusselt number ($Nu = \delta h / \lambda_g$) in that configuration, where δ is the characteristic length of the plate and λ_g is the thermal conductivity of air. In this case, the characteristic length δ is the ratio between surface *A* and perimeter *p* of the horizontal plate. Considering a perfectly square sample with 25 mm side, δ is 6.25 mm. Typical of free-convection boundary layer flows (Ref 40), the Rayleigh number (*Ra*), defined according to Eq 6, was also calculated to ultimately determine *Nu* by a $Nu = f(Ra)$ relationship:

$$Ra = \frac{g(T_{\text{surf}} - T_\infty)\delta^3}{\nu^2} Pr \tag{Eq 6}$$

where *g* is the gravitational acceleration (9.81 m/s²), *T_{surf}* was assumed as 150 °C (generally consistent with experimental conditions), *T_∞* was assumed as 25 °C (consistent with average ambient temperature in the test chamber), ν is the kinematic viscosity of air, and *Pr* is the Prandtl number of air. In the calculation of the convective heat transfer coefficient, all the thermophysical properties of air—*Pr* included—were evaluated at film temperature $T_f = (T_{\text{surf}} + T_\infty)/2$, defined as the arithmetic mean of the solid-boundary wall temperature and the free-stream gas temperature (Ref 40). The corresponding values are reported in Table 2. *Ra* turned out as equal to 1238. Finally, *Nu* could be calculated by the correlation developed by Corcione (Ref 41) for free-convection heat transfer of square plates in quiescent air and applicable in the $10^3 \leq Ra \leq 3 \times 10^7$ range:

Table 2 Thermophysical properties of air and film temperature employed for the calculation of convective heat transfer coefficient (Ref 38)

$T_f, ^\circ\text{C}$	$\lambda, \text{W}/(\text{m } ^\circ\text{C})$	$\nu, \text{m}^2/\text{s}$	Pr	$\beta, ^\circ\text{C}^{-1}$
63.50	0.0287	1.92917×10^{-05}	0.708	0.00297

$$\text{Nu} = 1.05 \text{Ra}^{0.215} \quad (\text{Eq 7})$$

As a result, $\text{Nu} = 4.85$ is obtained for the geometric, thermophysical and flow conditions considered here. The corresponding value for h is $23.6 \text{ W}/(\text{m}^2 \text{ } ^\circ\text{C})$, which is applied as boundary condition at the top and side surfaces.

The FE model was coded in ABAQUS 2016 and an implicit approach was employed to compute temperature and heat flux at each node and each time step (Ref 42). As opposed to other simulations of cooling of flat plates (Ref 29, 32), h was not recalculated at each time step to avoid raising computation time unnecessarily. A sensitivity analysis was performed against the FE code on the variation of h over a surface temperature range of $100\text{--}150 \text{ } ^\circ\text{C}$, which was deemed as a conservative estimate of the 60-s cooling. This analysis yielded surface temperature changes

in the order of $0.05 \text{ } ^\circ\text{C}$, thus supporting the choice of imposing constant h throughout the whole simulation.

Results and Discussion

As shown in Fig. 3, impact testing leaves visible marks with widespread defects on all samples; specifically on the top surface, circumferential cracks are formed along the boundary of the impact mark and radial cracks propagate away from the mark itself. Cross-sectional views (Fig. 4) show that the peripheral, circumferential cracks (label 1) extend through most of the coating thickness, though they do not reach the coating/substrate interface. At the center of the impact area, transverse cracks originating from the interface propagate vertically halfway across the coating thickness (label 2); however, they do not emerge at the outer surface (no central cracks appear at all in Fig. 3).

These cracking patterns resemble those found by the authors in a previous study on thermal spray metal layers (Ref 43) and are perfectly consistent with the location of tensile stress maxima in the coating during an impact event, as recently shown by FE simulations in the same work (Ref 43). The magnified detail provided in the inset

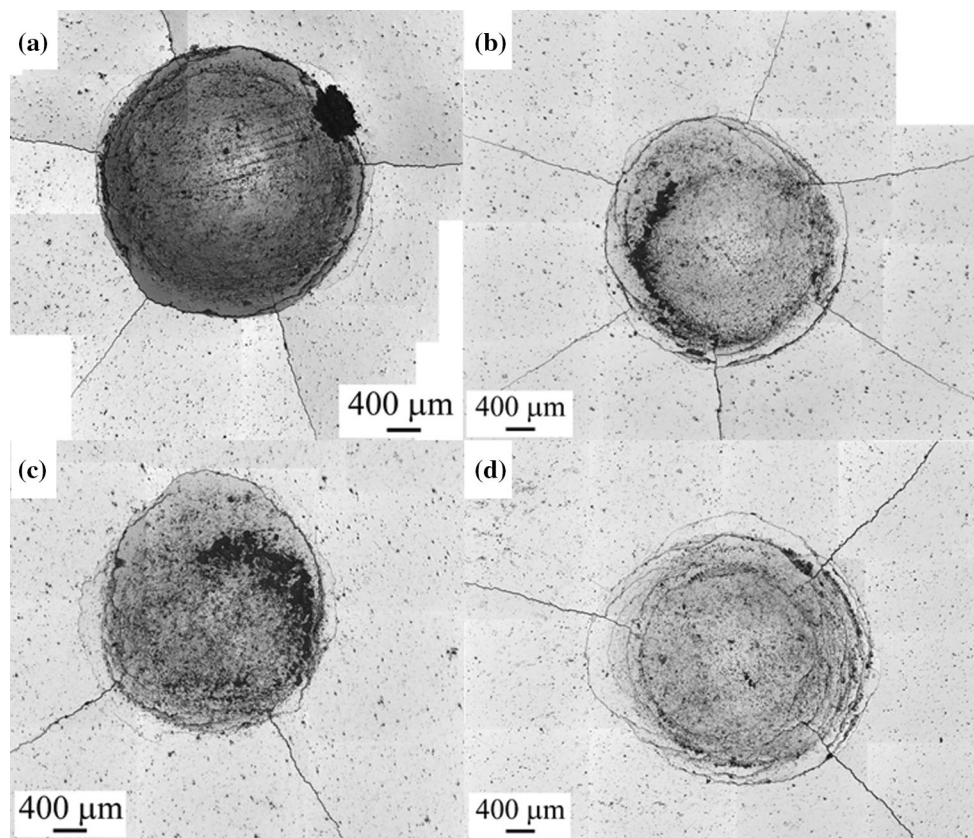


Fig. 3 Optical micrographs of impact marks on the surfaces of HVOF-sprayed Fe-Cr-Ni-B-C (a), HVOF-sprayed Fe-Cr-Ni-Mo-B-C (b), HVOF-sprayed Fe-Cr-Ni-Mo-B-C (c), HVOF-sprayed Fe-Cr-Ni-Mo-B-C (d)

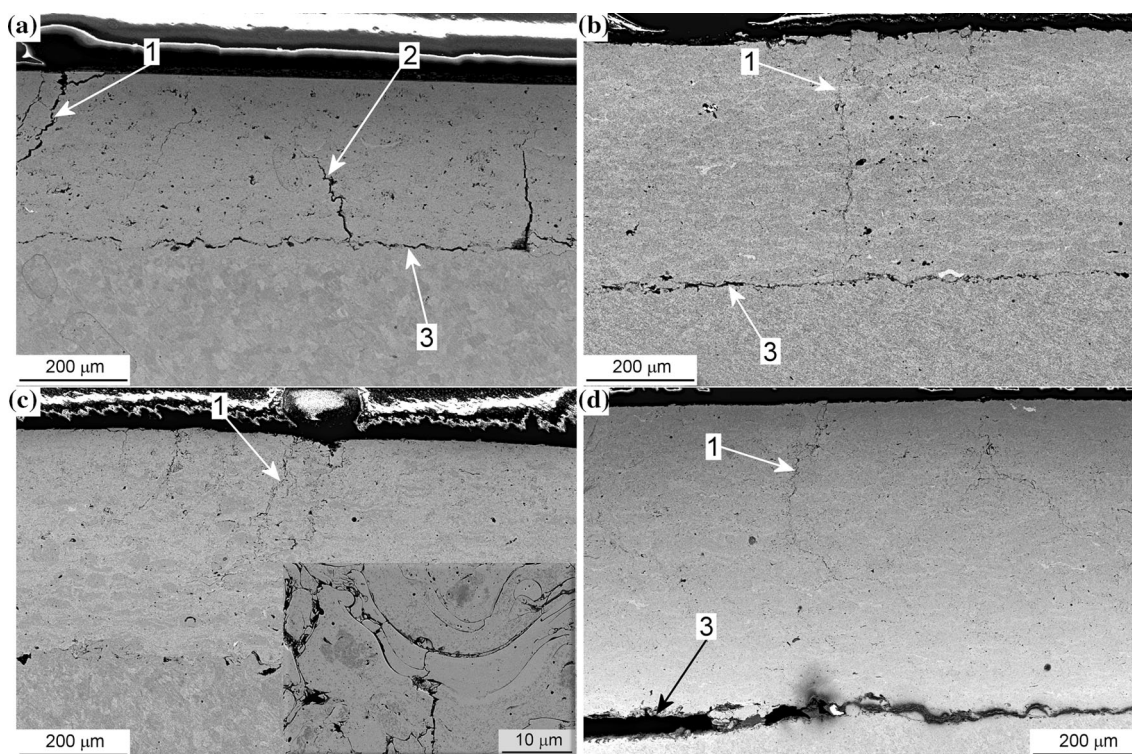


Fig. 4 FEG-SEM cross-sectional micrographs of impact-tested samples: HVOF-sprayed Fe-Cr-Ni-B-C (a), HVAF-sprayed Fe-Cr-Ni-B-C (b), HVOF-sprayed Fe-Cr-Ni-Mo-B-C (c), HVAF-sprayed Fe-Cr-Ni-

Mo-B-C (d); (1): circumferential crack, (2): central vertical cracks, (3): delamination crack

of Fig. 4(b) highlights that cracks propagate both around and across lamellae, depending on their interface cohesion as well as on intra-lamellar toughness. In fact, well-flattened, molten lamellae may adhere strongly to one another, but may also be internally embrittled by the formation of an amorphous, super-saturated solid solution (Ref 27).

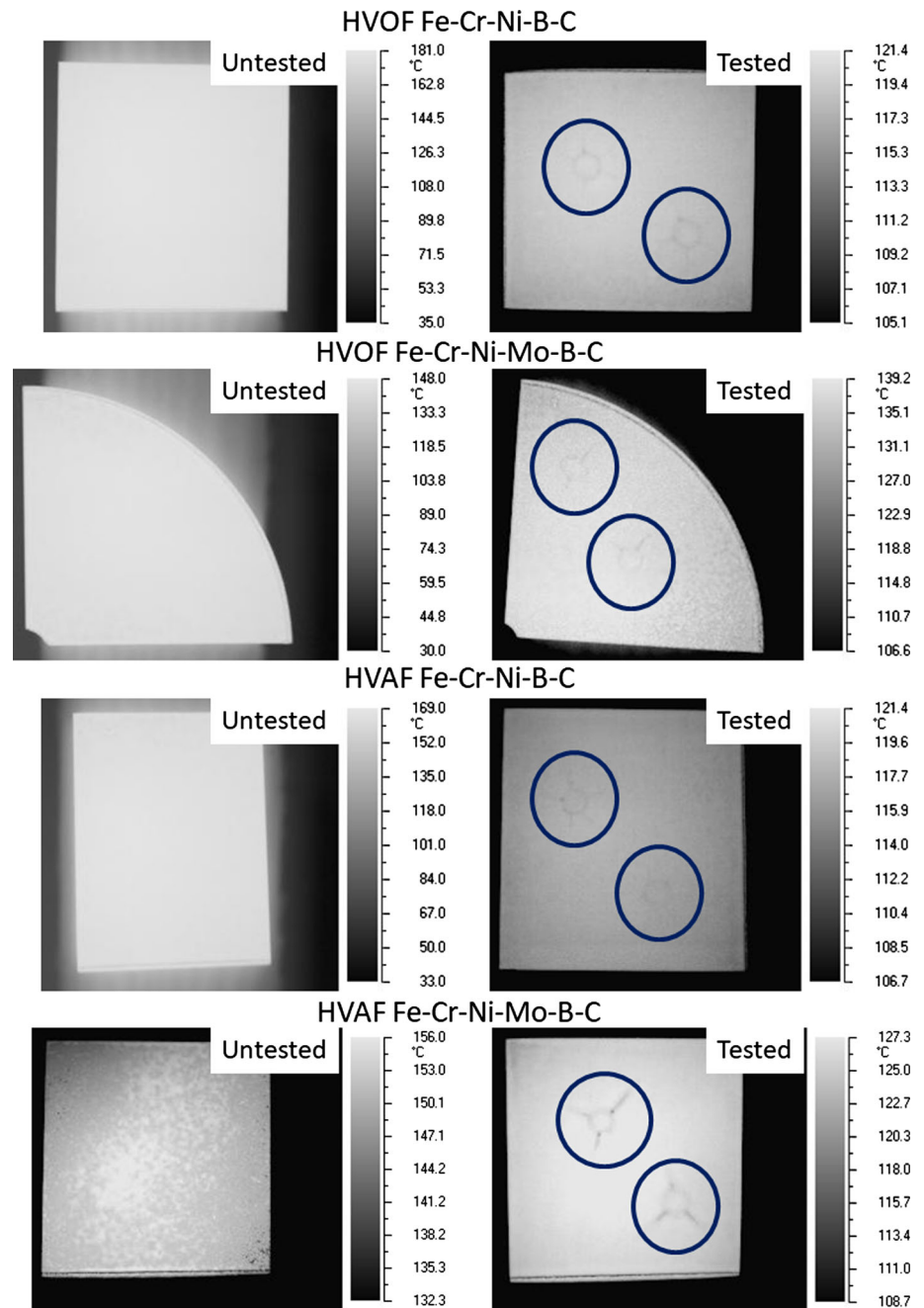
In addition, some of the coatings are delaminated from the substrate (Fig. 4a, c, and d: label 3), as the interface is highly stressed during impact, due to the difference in plastic deformability between the soft steel substrate and the harder coating (Ref 43). The extent of the delamination crack varies significantly among the tested samples, arguably due to their different residual stress states, to the mechanical and chemical compatibility between the coating and the substrate, etc. Studying the exact reasons for those differences exceeds the scopes of the present work; however, it is noted that these samples provide a representative damage variety against which the detection capabilities of IR thermography can be assessed.

As all of the radial, circumferential and delamination cracks seen in Fig. 3 and 4 are >1 mm long, the $115 \mu\text{m}$ /pixel resolution of thermographic images (“[Thermographic Testing: Instrumentation and Procedure](#)” section) appears suitable for their detection.

Thermographic images acquired on black-painted samples after heating and subsequent cooling for 60 s in quiescent air (Fig. 5) show that damage-free, untested samples exhibit uniform surface temperature. Therefore, the approach does not appear affected by any external signal or phenomenon—like surrounding light reflection mentioned in “[Thermographic Testing: Instrumentation and Procedure](#)” section—that might have otherwise led to incorrect identification of delamination damage.

On the tested samples, the visibility of impact marks in thermographic images (Fig. 5: circled areas) matches well with the actual extent of subsurface damage when compared to the corresponding SEM micrographs (Fig. 4). Almost no temperature inhomogeneity appears on the surface of the HVAF-sprayed Fe-Cr-Ni-B-C coating (Fig. 5), the only one showing almost no interface delamination crack (Fig. 4b): even around the boundary of the impact area, where most marked circumferential cracks are located, temperature differences are below 1°C . On the HVOF-sprayed coatings, which exhibit slight interface delamination (Fig. 4a and c), impact areas are somewhat more visible (Fig. 5) as they tend to become colder than the surrounding regions. Faster cooling of the impact area becomes particularly marked in the severely delaminated HVAF-sprayed Fe-Cr-Ni-Mo-B-C coating (Fig. 4d).

Fig. 5 Thermograms of the black-painted sample surface without (left) and with (right) impact damage (circled)



Especially around the boundary of the impact area, where circumferential and radial cracks combine, temperatures are up to ≈ 10 °C lower than in undamaged areas. This can be seen in the magnified view of the thermogram in Fig. 6, as well as in the corresponding temperature trends at locations around (points A, B) and away (point C) from the impact area. Accordingly, Table 3 shows quantitative differences between the highest temperature recorded on the sample surface (T_{\max} , corresponding to the temperature at point C) and the lowest one (T_{\min} , recorded at point A) at selected time steps during cooling (extracted from the thermograms).

Cross-sectional temperature contour maps from FE simulations (Fig. 6) demonstrate that in the damaged area convective cooling of the coating by surrounding air occurs faster than its heating by conduction from the hot substrate, due to the insulating effect of the interface crack. This explains why impact marks become clearer as interface cracks grow larger. The circumferential crack synergistically enhances this effect by hindering heat conduction from undamaged coating areas, which ultimately results in the thermographic snapshots and temperature recordings of Fig. 5 and 6.

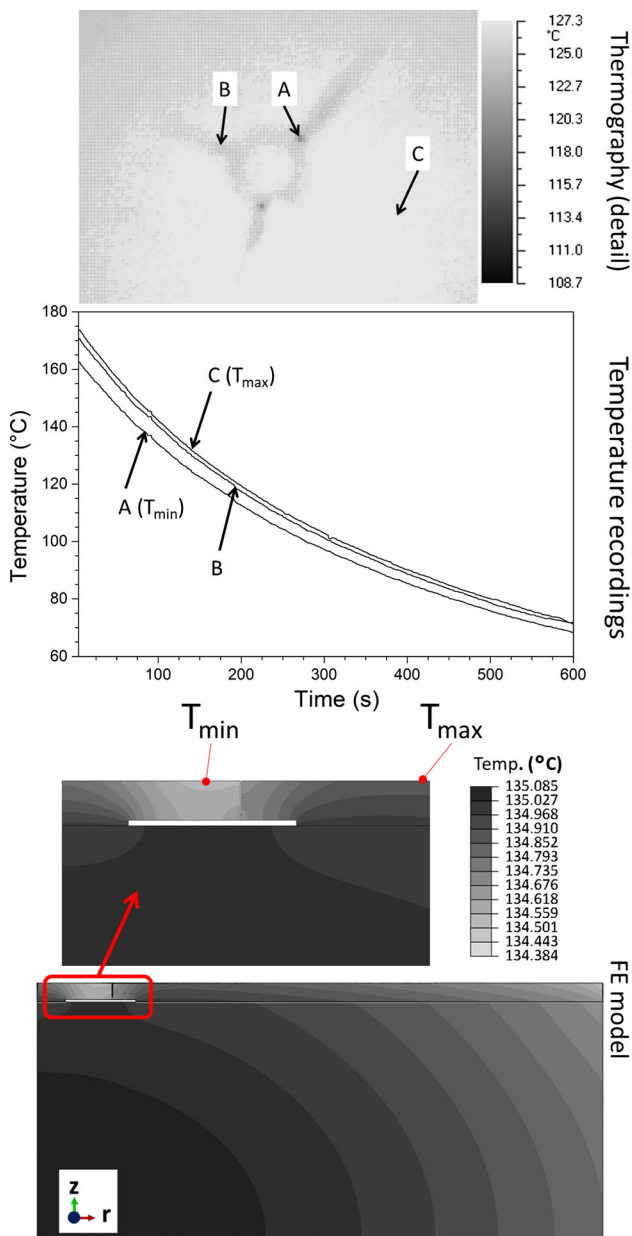


Fig. 6 Detail of the thermogram of the HVAF-sprayed Fe-Cr-Ni-Mo-B-C coating surface after 60-s cooling time (top), temperature evolution at the three marked points (full recording, center) and temperature contour map across a coated sample heated up to 150 °C and cooled for about 60 s (bottom)

According to the FE model, the difference between the highest and lowest temperatures (T_{max} and T_{min} , respectively: see Fig. 6) on the outer surface of the HVAF-sprayed Fe-Cr-Ni-Mo-B-C coating (<1 °C) is lower than the experimental one (Table 3). Firstly, this is due to some approximate values for thermal properties of the coating—as discussed in “Finite-Element Approach” section with relation to Table 1—and secondly and most importantly to the simplified model that does not include multiple circumferential cracks and additional radial, outward-

Table 3 Experimentally measured temperature difference between the hottest (T_{max}) and coldest (T_{min}) points on the surface of the HVAF-sprayed Fe-Cr-Ni-Mo-B-C coating, compared to the predictions of the FE model at various times (see Fig. 6)

Time, s	$T_{max} - T_{min}$, °C experimental	$T_{max} - T_{min}$, °C FE model
0	0	0
15	10.7	0.25
30	10.3	0.25
45	9.7	0.24
60	9.3	0.24
90	8.4	0.23
120	7.8	0.21

branching cracks. These latter further reduce heat transfer to the damaged areas. Away from those radial cracks, the thermogram of Fig. 5 and its detailed version in Fig. 6 indeed show a temperature difference of about 1 °C between the areas adjacent to the circumferential cracks and the undamaged ones, closer to the model prediction.

In order improve the quantitative accuracy of the FE simulations, a high-resolution three-dimensional (3D) model may be developed and implemented: that would allow capturing all damage features with high spatial accuracy. This resource-intensive effort might require the use of techniques such as 3D micro-tomography to perform quantitative model validation or to provide it with input about microstructure and crack patterns, as recently shown by Li et al. (Ref 44). This approach lies beyond the scopes of the present investigation. Even under the aforementioned approximations, the FE code proposed here implements a fully physical set of relationships, so the qualitative consistency between computed and measured surface temperature distribution allows considering IR thermography of black-painted samples as a reliable and fairly unbiased methodology. The IR-thermography approach appears robust even from a quantitative standpoint, given its rather simple features (“Thermographic Testing: Instrumentation and Procedure” section).

Depositing an ethanol droplet onto one of the crack locations (Fig. 7a and b) seems to provide a mild yet perceivable amplified effect on crack visualization. After the “cold halo” produced immediately after vaporization (Fig. 7c) has been dissipated, the crack with the droplet deposited onto (Fig. 7d—label 1) appears overall more emphasized than the other one (Fig. 7d—label 2). Notably, the crack region with the ethanol droplet previously released onto presents a temperature difference with respect to undamaged areas of about 20 °C, whereas the same difference for the undisturbed crack region is about 10 °C, as noted previously (Fig. 7d). However, one drawback affects this particular approach: radial cracks in the

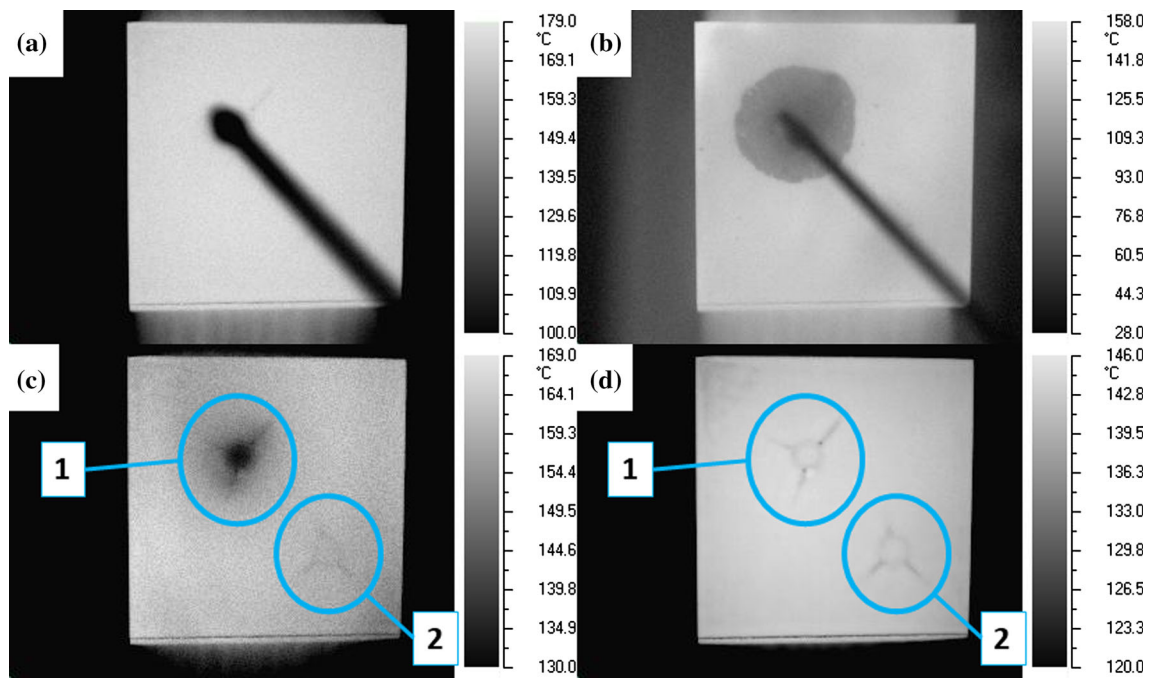


Fig. 7 IR thermographic sequence of the black-painted HVAF-sprayed Fe-Cr-Ni-Mo-B-C sample surface with an ethanol droplet deposited onto one of the crack locations (emissivity set as 0.95): prior to deposition, with the employed syringe clearly visible (a);

during deposition (b); immediately after ethanol evaporation (c); 50 s after ethanol evaporation (d). Label 1 = impact area perturbed by ethanol drop; label 2 = unperturbed impact area

deposition region appear coarser than in the remaining part of the sample surface (Fig. 7c and d), which is arguably due to the overlapping effects of droplet evaporation and cooling of damaged areas. Moreover, releasing an ethanol droplet appears more appropriate for research purpose, rather than for industrial applications, since the use of alcohol on heated bodies may result in undesired safety issues. However, this approach seems promising and may yield remarkable improvements, especially through a more comprehensive selection of deposition methods and deposited fluids.

On the other hand, using untreated (not black-painted) samples makes thermographic results less clear (Fig. 8). Three distinct issues arise from this study:

1. The emissivity of the polished coating surface is not known precisely. As remarked in “[Thermographic Testing: Instrumentation and Procedure](#)” section, the 0.20 value is indeed an approximation, even though supported by data available for similar materials. Therefore, temperature values in the thermographic images of untreated samples are affected by significant uncertainty. By contrast, thermograms of black-painted sample surfaces are reliable from a quantitative standpoint, although the detection of defects and delamination cracks through “cold spots” relies on qualitative evaluations of temperature patterns rather

than on absolute values. Namely, the authors do not propose the use of quantitative temperature thresholds for the identification of “cold spots”;

2. Reflection of surrounding irradiation and light from the polished coating surface results in further quantitative bias to the IR images and produces artifacts, such as the seemingly “colder” area appearing in the central portion of the unpainted sample of Fig. 8, which are absent in thermographic snapshots of the black-painted sample. These artefacts resemble the disturbing signals that affected identification of actual delamination damage in the IR thermograms of thermal spray aluminum reported by Murariu et al. (Ref 20). Probably, the disturbances found in that study have the same origin as the present one. This stresses the importance of applying a black-paint layer in the IR-thermography procedure;
3. Surface emissivity is locally altered by any residue left by contact with the counterbody in a tribological coupling and or by any corrosion product, which would probably be a frequently recurring issue in practical applications. All those phenomena may yield inhomogeneous emissivity of the whole surface. Some material transfer from the impacting ball to the coating surface did occur in the present experiments, which appears in the form of dark material clusters lying onto

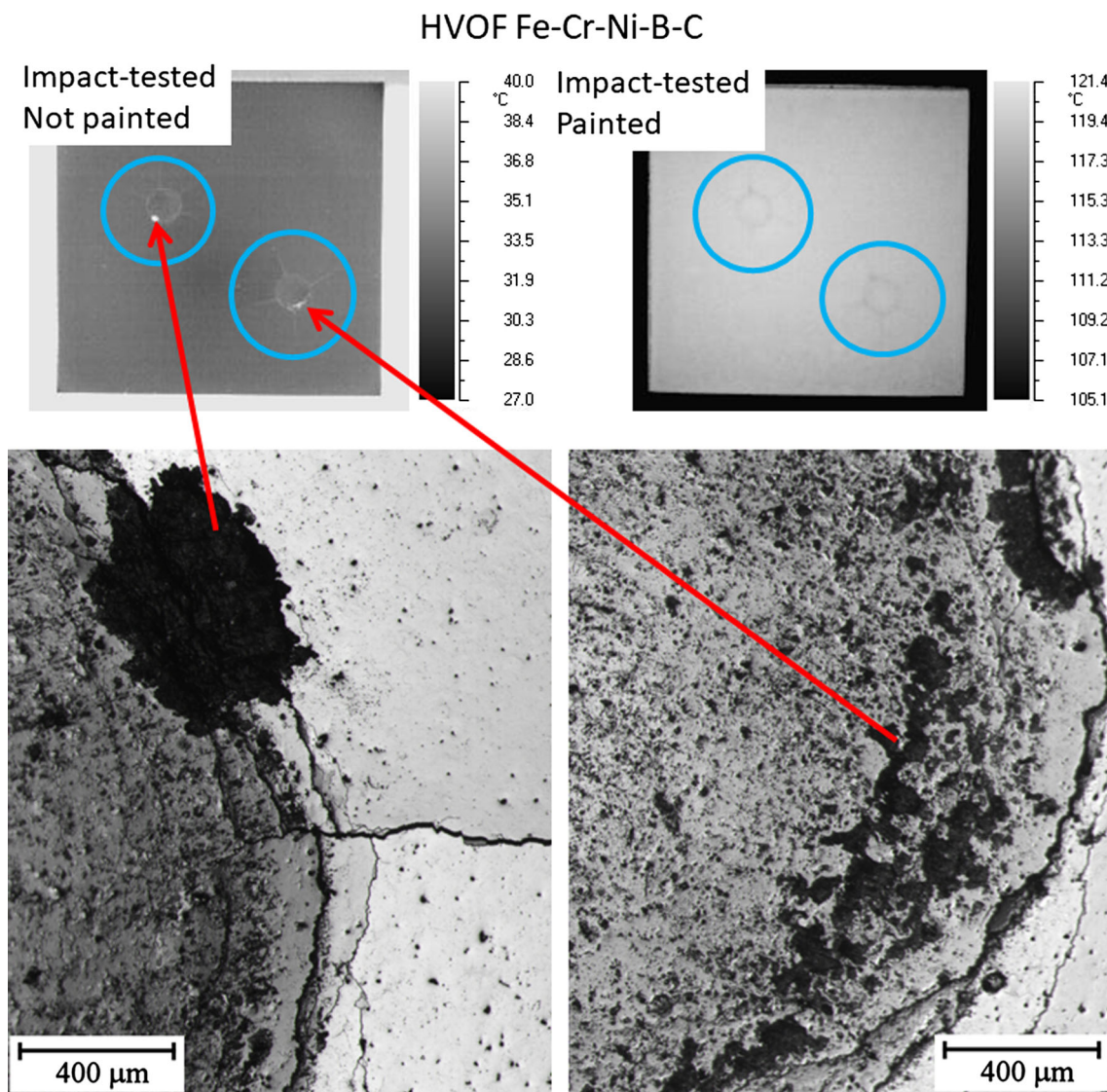


Fig. 8 Comparison between thermograms acquired on the HVOF-sprayed Fe-Cr-Ni-B-C surface with impact damage (circled), after about 60 s cooling from above 100 °C, without and with the black-

paint layer. Optical micrographs show clusters of transfer material in the locations corresponding to “hot spots” in the thermogram of the sample without paint

the impact marks in Fig. 2. Areas with locally different emissivity on an isothermal surface generate a visual temperature difference in post-processed thermographic images, which can be easily misinterpreted as actual “hot” or “cold” spots. For instance, in Fig. 8 the arrows mark two seemingly “hot” spots in the impact marks on HVOF-sprayed Fe-Cr-Ni-B-C, which do not correspond to any actual subsurface damage; in fact, they correspond to residues of transferred material, as revealed by corresponding optical micrographs. These artefacts are resolved as the related clusters are covered by black paint, so that a surface with certain and uniform emissivity is obtained.

Conclusions

This work shows the applicability of IR thermography as a non-destructive technique to detect the presence of subsurface impact damage in thermal spray metallic coatings. A particularly simple and inexpensive procedure was implemented, which consists of bulk heating the entire sample using an IR lamp and then monitoring the surface transient cooling by an IR thermocamera. With this setup, failed coating regions show up as “cold spots” in thermographic images, as opposed to works employing similar imaging techniques under flash heating (Ref 10-16), where “hot spots” were found instead. A FE model was also developed as fully based on physical relationships to challenge the experimental approach in capturing the

surface temperature trend. The simulations indeed show that damaged regions are convectively cooled by surrounding air faster than they are heated by conduction from the hot substrate, due to the insulating effect of subsurface damages. That supports and explains the visualization of colder regions corresponding to cracks (particularly to interface delamination cracks) in IR snapshots. A FEG-SEM analysis of the samples after IR-thermography tests was conducted, showing excellent agreement between the experimental and numerical approaches in determining crack location.

The IR-thermography-based procedure can be employed for small- and medium-scale components both for industrial and for research purposes. For instance, failed samples could be rapidly identified within a vast experimental campaign, avoiding systematic, destructive and time-consuming metallographic inspection.

Although the temperature differences between failed and intact coating portions are of the order of few degrees Celsius, they can be effectively and reliably detected by currently available thermocameras. The use of a thin layer of acrylic black paint applied onto the coating upper surface is instrumental in enhancing and homogenizing surface emissivity to a known value, thus avoiding artificial “hot” and “cold” spots and quantitative uncertainties on measured temperature values. Those biases and uncertainties were clearly found in IR-thermography analysis of untreated coating surfaces. The paint is soluble in acetone; hence, it can be removed from the sample after inspection.

Rather interestingly, deposition of ethanol droplets onto black-painted surfaces proved promising in quantitatively emphasizing the visualization of cracks once the droplet is evaporated, yet this particular approach appears less precise in evaluating the spatial extent of damaged regions.

Further research should address adaptations to large-sized parts, including: (1) devising a black paint that can be removed with a less harmful solvent than acetone, the use of which is impractical onto large surfaces and unsafe, (2) employing flash or laser heating where bulk heating might be unfeasible and (3) developing means to scan efficiently the entire component surface.

Moreover, the deposition of different fluids onto black-painted coating surfaces may be tested to keep the same visualization enhancing effect, while avoiding safety issues due to alcohol flammability.

Acknowledgments The authors wish to thank Prof. P. Tartarini (Università degli Studi di Modena e Reggio Emilia, Italy) for providing IR-thermography instrumentation. Mr. G. Urso and CIGS (Centro Interdipartimentale Grandi Strumenti) at Università degli Studi di Modena e Reggio Emilia, Italy, are also acknowledged.

References

1. C. Liebert and F.S. Stepka, Ceramic Thermal-Barrier Coatings for Cooled Turbines, *J. Aircr.*, 1977, **14**(5), p 487-493
2. J.T. DeMasi-Marcin and D.K. Gupta, Protective Coatings in the Gas Turbine Engine, *Surf. Coat. Technol.*, 1994, **68**, p 1-9
3. D.R. Clarke and S.R. Phillpot, Thermal Barrier Coating Materials, *Mater. Today*, 2005, **8**(6), p 22-29
4. R.C. Tucker, Ed., Existing and New Market Opportunities in Thermal Spray Applications, *ASM Handbook—Volume 5A: Thermal Spray Technology*, (Materials Park, OH, USA), ASM International, 2013, p 243-337
5. C.-J. Li and A. Ohmori, Relationships between the Microstructure and Properties of Thermally Sprayed Deposits, *J. Therm. Spray Technol.*, 2002, **11**(3), p 365-374
6. Y.-Y. Wang, C.-J. Li, and A. Ohmori, Influence of Substrate Roughness on the Bonding Mechanisms of High Velocity Oxy-Fuel Sprayed Coatings, *Thin Solid Films*, 2005, **485**(1), p 141-147
7. W.J. Trompetter, A. Markwitz, M. Hyland, and P. Munroe, Evidence of Mechanical Interlocking of NiCr Particles Thermally Sprayed onto Al Substrates, *J. Therm. Spray Technol.*, 2005, **14**(4), p 524-529
8. W. Riggs, D. Rucker, and K. Couch, Testing of Coatings, *ASM Handbook—Volume 5A: Thermal Spray Technology*, R.C. Tucker, Ed., (Materials Park, OH, USA), ASM International, 2013, p 214-237
9. L. Pawlowski, *The Science and Engineering of Thermal Spray Coatings*, 2nd ed., Wiley, Chichester, 2008
10. S. Zhao, H. Wang, N. Wu, and C. Zhang, Nondestructive Testing of the Fatigue Properties of Air Plasma Sprayed Thermal Barrier Coatings by Pulsed Thermography, *Rus. J. Nondestruct. Test.*, 2015, **51**(7), p 445-456
11. M. Seraffon, N.J. Simms, J.R. Nicholls, J. Sumner, and J. Nunn, Performance of Thermal Barrier Coatings in Industrial Gas Turbine Conditions, *Mater. High Temp.*, 2011, **28**(4), p 309-314
12. S.B. Zhao, C.L. Zhang, N.M. Wu, and H.M. Wang, Quality Evaluation for Air Plasma Spray Thermal Barrier Coatings with Pulsed Thermography, *Prog. Natl. Sci. Int. Chin. Mater. Res. Soc.*, 2011, **21**(4), p 301-306
13. V.C. Dina, G.M. Dumitru, and C. Dumitrascu, The Un Destructive Examination by Active Pulse Thermography of the Layers Deposited by Thermal Spraying, *Appl. Mech. Mater.*, 2013, **325-326**, p 371-374
14. Q. Tang, J. Liu, J. Dai, and Z. Yu, Theoretical and Experimental Study on Thermal Barrier Coating (TBC) Uneven Thickness Detection Using Pulsed Infrared Thermography Technology, *Appl. Therm. Eng.*, 2016, **114**, p 770-775
15. M. Schweda, T. Beck, M. Offermann, and L. Singheiser, Thermographic Analysis and Modelling of the Delamination Crack Growth in a Thermal Barrier Coating on Fecralloy Substrate, *Surf. Coat. Technol.*, 2013, **217**, p 124-128
16. T. Ahmed, Z.J. Feng, P.K. Kuo, J. Hartikainen, and J. Jaarinen, Characterization of Plasma Sprayed Coatings Using Thermal Wave Infrared Video Imaging, *J. Nondestruct. Eval.*, 1987, **6**(4), p 169-175
17. J.T. Demasi-Marcin, K.D. Sheffler, and S. Bose, “Mechanisms of Degradation and Failure in a Plasma Deposited Thermal Barrier Coating,” *ASME 1989 International Gas Turbine and Aeroengine Congress and Exposition—Volume 5*, 1989, p V005T12A004
18. S. Chaki, P. Marical, S. Panier, G. Bourse, and A. Mouftiez, Interfacial Defects Detection in Plasma-Sprayed Ceramic Coating Components Using Two Stimulated Infrared Thermography Techniques, *NDT E Int.*, 2011, **44**(6), p 519-522

19. H. Reed and W. Hoppe, A Model-Based, Bayesian Characterization of Subsurface Corrosion Parameters in Composite Multi-Layered Structures, *AIP Conf. Proc.*, 2016, **1706**(1), p 120010
20. A.C. Murariu, S. Crăsteți, and A.V. Birdeanu, Active Infrared Thermography Method for Non-Destructive Examination of Coating Layers, *Struct. Integr. Life*, 2016, **16**(1), p 3-8
21. A.C. Murariu and S. Crasteti, Nondestructive Assessment of Anticorrosive Aluminium Coatings by Active Infrared Thermography, *Adv. Mater. Res.*, 2013, **814**, p 235-243
22. A. Bendada, Nondestructive Inspection of Scuff-Resistant Coating Adhesion Flaws in Automobile Engine Block Cylinders, *J. Adhes. Sci. Technol.*, 2004, **18**(8), p 943-950
23. M. Dvorak, C. Florin, and E. Amrhein, "Online Quality Control of Thermally Sprayed Coatings," *Thermal Spray 2001: New Surfaces for a New Millennium—Proceedings of the International Thermal Spray Conference*, C.C. Berndt, K.A. Khor, and E. Lugscheider, Eds., (Materials Park, OH, USA), ASM International, 2011, p 1255-1259
24. J. Délémontez, M. Taglione, A. Rivière, and E. Martin, "Inspection of HVOF-Coated Pelton Wheels Using Active Thermography", *Quantitative InfraRed Thermograph Conference*, 2014.
25. F. Cernuschi, P. Bison, S. Marinetti, and E. Campagnoli, Thermal Diffusivity Measurement by Thermographic Technique for the Non-destructive Integrity Assessment of TBCs Coupons, *Surf. Coat. Technol.*, 2010, **205**(2), p 498-505
26. J. Nunn, S. Saunders, and J. Banks, Application of Thermography in the Evaluation of Early Signs of Failure of Thermal Barrier Coating Systems, *Mater. High Temp.*, 2005, **22**(3/4), p 385-392
27. A. Milanti, V. Matikainen, G. Bolelli, H. Koivuluoto, L. Lusvarghi, and P. Vuoristo, Microstructure and Sliding Wear Behavior of Fe-Based Coatings Manufactured with HVOF and HVOF Thermal Spray Processes, *J. Therm. Spray Technol.*, 2016, **25**(5), p 1040-1055
28. M. Barletta, G. Bolelli, B. Bonferroni, and L. Lusvarghi, Wear and Corrosion Behavior of HVOF-Sprayed WC-CoCr Coatings on Al Alloys, *J. Therm. Spray Technol.*, 2009, **19**(1), p 358-367
29. P.E. Santangelo, M.A. Corticelli, and P. Tartarini, Spray Cooling by Gently-Deposited Droplets: Experiments and Modeling of Heat-Transfer Mechanisms, *15th International Heat Transfer Conference*, (Kyoto, Japan), 2014, p IHTC15-8367
30. P.E. Santangelo, A.W. Marshall, P. Valdiserri, B. Pulvirenti, and P. Tartarini, Fire Suppression by Water-Mist Sprays: Experimental and Numerical Analysis, *14th International Heat Transfer Conference, Volume 5*, (Washington, DC, USA), ASME Heat Transfer Division, 2010, p 571-580
31. P. Tartarini, M.A. Corticelli, and P.E. Santangelo, Experimental and Numerical Analysis of Droplet Cooling, *14th International Heat Transfer Conference, Volume 6*, (Washington, DC, USA), ASME Heat Transfer Division, 2010, p 677-685
32. P.E. Santangelo, M.A. Corticelli, and P. Tartarini, Experimental and Numerical Analysis of Thermal Interaction between Two Droplets in Spray Cooling of Heated Surfaces, *Heat Transf. Eng.*, 2017. doi:10.1080/01457632.2017.1295737
33. F.P. Incropera and D.P. DeWitt, *Fundamentals of Heat and Mass Transfer*, Wiley, New York, 1981
34. Emissivity Values for Common Materials. <http://www.infrared-thermography.com/material.htm>. Accessed 3 June 2017
35. M. Klassen, M. di Marzo, and J. Sirkis, Infrared Thermography of Dropwise Evaporated Cooling, *Exp. Therm. Fluid Sci.*, 1992, **5**(1), p 136-141
36. Ethanol. <http://webbook.nist.gov/cgi/cbook.cgi?ID=C64175&Type=IR-SPEC&Index=2>. Accessed 3 June 2017
37. A. Ibrahimbegović, Quadrilateral Finite Elements for Analysis of Thick and Thin Plates, *Comput. Methods Appl. Mech. Eng.*, 1993, **110**(3-4), p 195-209
38. Air Properties. http://www.engineeringtoolbox.com/air-properties-d_156.html. Accessed 30 April 2017
39. J.A. Garcia, A. Mandelis, B. Farahbakhsh, C. Lebowitz, and I. Harris, Thermophysical Properties of Thermal Sprayed Coatings on Carbon Steel Substrates by Photothermal Radiometry, *Int. J. Thermophys.*, 1999, **20**(5), p 1587-1602
40. L.M. Jiji, *Heat Convection*, 2nd ed., Springer, Berlin, 2009
41. M. Corcione, Heat Transfer Correlations for Free Convection from Upward-Facing Horizontal Rectangular Surfaces, *WSEAS Trans. Heat Mass Transf.*, 2007, **2**(3), p 48-60
42. S.V. Patankar, *Numerical Heat Transfer and Fluid Flow*, Hemisphere Publishing Corporation, Washington, DC, USA, 1980
43. G. Bolelli, A. Milanti, L. Lusvarghi, L. Trombi, H. Koivuluoto, and P. Vuoristo, Wear and Impact Behaviour of High Velocity Air-Fuel Sprayed Fe-Cr-Ni-B-C Alloy Coatings, *Tribol. Int.*, 2016, **95**, p 372-390
44. C. Li, X. Zhang, Y. Chen, J. Carr, S. Jacques, J. Behnsen, M. di Michiel, P. Xiao, and R. Cernik, Understanding the Residual Stress Distribution through the Thickness of Atmosphere Plasma Sprayed (APS) Thermal Barrier Coatings (TBCs) by High Energy Synchrotron XRD; Digital Image Correlation (DIC) and Image Based Modelling, *Acta Mater.*, 2017, **132**, p 1-12